Solidus Surface of the Mo–Fe–B System

Article *in* Powder Metallurgy and Metal Ceramics · July 2020

DOI: 10.1007/s11106-020-00141-w

5 authors, including:

A. A. Bondar
National Academy of Sciences of Ukraine
1,091 PUBLICATIONS **27,395** CITATIONS

SEE PROFILE

Ira Tihonova
National Academy of Sciences of Ukraine
5 PUBLICATIONS **15** CITATIONS

SEE PROFILE

DOI 10.1007/s11106-020-00141-w
Powder Metallurgy and Metal Ceramics, Vol. 59, Nos. 1-2, May, 2020 (Russian Original Vol. 59, Nos. 1-2, Jan.-Feb., 2020)

PHYSICOCHEMICAL MATERIALS RESEARCH

SOLIDUS SURFACE OF THE Mo–Fe–B SYSTEM

S.V. Utkin,[1] A.A. Bondar,[1,3] V.Z. Kublii,[1] L.M. Kapitanchuk,[2] and I.B. Tikhonova[1]

UDC 669.017

The arc-melted Mo–Fe–B alloys with boron content up to ~41 at.% were studied after annealing at subsolidus temperatures by X-ray diffraction, differential thermal analysis, SEM/EMPA, and Pirani–Altertum technique for measurement of incipient melting temperatures. The partial solidus surface projection was constructed for the first time in the Mo–$MoB_{1.0}$–$FeB_{\sim 0.8}$–Fe region using our own experimental and literature data. The Mo_2FeB_2 ternary compound has a two-phase equilibrium at subsolidus temperatures with each of the binary and unary phases from the constituent binary systems. The Mo_2FeB_2 phase has a wide homogeneity range for metal content: 14–27 at.% Fe. A three-phase α-MoB + β-MoB + Mo_2B region exists close to the Mo–B side of the Gibbs composition triangle. In addition, a three-phase region composed by the Mo_2FeB_2 ternary compound and two iron modifications is shown to exist: BCC (δ-Fe) and FCC (γ-Fe). Another ternary compound, $Mo_xFe_{3-x}B$, with molybdenum content of 1.3–2.0 at.% is present at subsolidus temperatures in two structural modifications: orthorhombic (Fe_3C-type structure) and tetragonal (Ti_3P-type structure). The intermetallic μ-(Mo_6Fe_7) phase in the Mo–Fe–B ternary system takes part in the three-phase equilibria on the solidus surface: σ-(MoFe) + μ-(Mo_6Fe_7) + Mo_2FeB_2 at 1375 ± ± 10°C, μ-(Mo_6Fe_7) + Mo_2FeB_2 + R-(Mo_2Fe_3) at 1340 ± 10°C, and σ-(MoFe) + μ-(Mo_6Fe_7) + R-(Mo_2Fe_3) at 1385 ± 10°C.

Keywords: *B–Mo–Fe, phase diagram, solidus, ternary boride, Mo_2FeB_2.*

INTRODUCTION

The Mo–Fe–B ternary system is of interest as it serves as a basis for developing tungsten-free hardmetals [1] and boride wear-resistant and corrosion-resistant coatings [2] from ternary Mo_2FeB_2 boride. The Vickers microhardness of Mo_2FeB_2 is 23.1 ± 1.4 GPa according to [3] and 20–26 GPa according to our measurements. The paper [2] reports on the production of a protective coating from complex $Mo_2(Fe,Ni)B_2$ boride, which has 84–85 HRA hardness and good adhesion to a steel substrate. Complex borides find application as strengthening and protective coatings on magnetic tapes [4] and as materials for walls of baths with molten zinc [5]. The Mo–Fe–B

[1]Frantsevich Institute for Problems of Materials Science, National Academy of Sciences of Ukraine, Kyiv, Ukraine. [2]Paton Electric Welding Institute, National Academy of Sciences of Ukraine, Kyiv, Ukraine.
[3]To whom correspondence should be addressed; e-mail: aa_bondar@ukr.net.

Translated from Poroshkova Metallurgiya, Vol. 59, Nos. 1–2 (531), pp. 121–139, 2020. Original article submitted July 3, 2019.

TABLE 1. Crystallographic Characteristics of

Phase	Temperature of existence, °C	Pearson symbol	Space group	Prototype
α, δ, (αδ-Fe)	<912; 1394–1538	*cI*2	$Im\bar{3}m$	W
γ, (γ-Fe)	912–1394	*CF*4	$Fm\bar{3}m$	Cu
(Mo)	<2623	*cI*2	$Im\bar{3}m$	W
FeB	<1603	*oP*8	*Pnma*	FeB
Fe_2B	<1399	*tI*12	*I*4/*mcm*	$CuAl_2$
Fe_3B	Metastable	*tI*32	$I\bar{4}$	Ni_3P
Fe_3B	Metastable	*tP*32	$Fe_3P_{0.37}B_{0.63}$	Ti_3P
Fe_3B	Metastable	*oP*16	*Pnma*	Fe_3C
σ, MoFe	1611–1235	*tP*30	$P4_2/mnm$	σ-CrFe
μ, Mo_6Fe_7	<1370	*hR*13	$R\bar{3}m$	W_6Fe_7
R, Mo_2Fe_3	1488–1200	*hR*53	$R\bar{3}m$	R-(Co ,Cr, Mo)
λ, $MoFe_2$	<927	*hP*12	$P6_3/mmc$	$MgZn_2$
β-MoB	2600–1800	*oC*8	*C mcm*	CrB
α-MoB	<2180	*tI*16	$I4_1/amd$	α-MoB
Mo_2B	<2280	*tI*12	*I*4/*mcm*	$CuAl_2$
τ_1, $Mo_2Fe_{13}B_5$ $Mo_{0.2}Fe_{2.8}B_3$	1000–1100 1050–1110	*tP*32	$P4_2/n$	Ti_3P
τ_2, Mo_2FeB_2	1000–1050	*tP*10	*P*4/*mbm*	U_3Si_2
τ_3, $Mo_{1-x}Fe_xB$		*oC*8	*Cmcm*	CrB
τ_4, $Mo_{1+x}Fe_{2-x}B_4$, $x = 0–1$		*oI*14	*Immm*	Ta_3B_4

Lattice parameters, pm			Comments, references
a	*b*	*c*	
286.65	–	–	At 25°C [12]
364.67	–	–	At 915°C [12, 13], dissolves 1.7 at.% Mo at 1140°C [14]
314.70	–	–	At 25°C [12], dissolves <0.4 at.% B at 2148°C [15] and 26.6 at.% Fe at 1612°C [14]
550.6	295.2	406.1	50 at.% B [13]
511.0		490.9	33.3 at.% B [13]
865.5	–	429.7	Disordered high-temperature modification, resulting from quenching of the $Fe_{76}B_{24}$ melt at 1150–1250°C [16]
864.8	–	431.4	Ordered low-temperature modification [16]
443.9	542.8	669.9	Coexists with low-temperature modification in rapidly quenched alloys [16]
918.8	–	481.2	[12, 17] 44.5–52.1 at.% Fe [14]
475.46	–	2571.6	[12, 13] 55.7–60.8 at.% Fe [14]
1091.0	–	1935.4	[12] 63.9–64.2 at.% Fe [14] $Mo_{1.9}Fe_{3.1}$ at 1250–1490°C [13]
475.5	–	776.7	[12, 13] 66.3 at.% Fe [14]
314.02	848.9	307.1	[18] 48.6–50.8 at.% B [15]
310.68	–	1696.18	[18] 48.3–50.2 at.% B [15]
554.8	–	474.06	[18] 32.6–33.7 at.% B [15]
863.4 863.17(7)	–	428.1 431.31	After annealing at 1050°C [19] [20]
578.2 580.7 577.26	–	314.8 314.2 314.61	[21] After annealing at 1000°C [22] After annealing at 1050°C [20]
315.26	841.86	306.62	After annealing at 1050°C [20]
299.6	1279	309.9	$x = 0.06$; annealed at 1050°C [20]

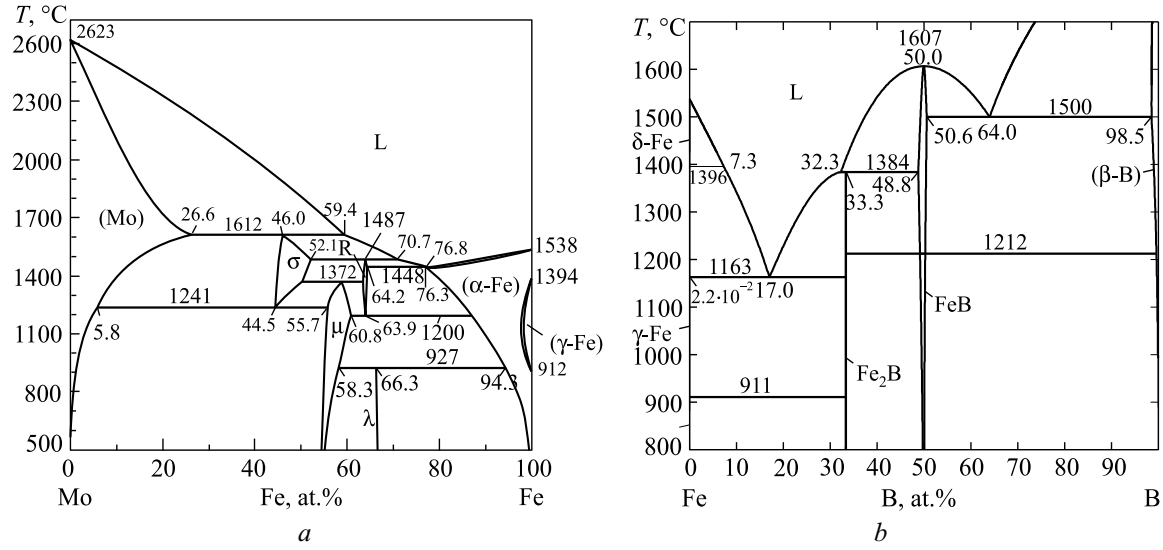

Fig. 1. The Mo–Fe [14] (*a*) and Fe–B [27] (*b*) phase diagrams

alloys tend to glass formation in the iron-rich region [6, 7] and have interesting magnetic properties [8, 9]. The literature reports that microdoping with boron is an important method to modify the structure and facilitate the sintering of steel powders [10, 11], while the effect of boron macrodoping on the properties of iron-based alloys still has to be examined.

The binary systems that constitute the Mo–Fe–B system have been studied adequately. The crystallographic data for the phases are summarized in Table 1. We accepted the Mo–Fe phase diagram (Fig. 1*a*) upon thermodynamic modeling (CALPHAD) [14]; it does not significantly differ from the version [23] accepted in the reference books [12, 24]. The Fe–B phase diagram in [25] includes Fe_3B boride, which we consider to be stable in the temperature range 1150–1250°C (in line with the papers [16, 26]) contrastingly to [12] et al. Hence, analysis of the literature data [27] shows that there is adequate evidence of the Fe_3B metastable nature. For the Fe–B and Mo–B systems, we accepted the versions of phase diagrams constructed using thermodynamic modeling and calculation (CALPHAD): for the Fe–B system according to [27] (Fig. 1*b*) and for the Mo–B system according to [15] (phase diagram provided in [28]).

Phase equilibria in the ternary Mo–Fe–B system have been mostly studied in solid state. The research results for this system obtained up to 2005 are summarized in [29]. The isothermal sections at 1000 and 1050°C were first constructed in [19, 22] using research results for annealed alloys melted in an arc furnace.

The isothermal section of the Mo–Fe–B system at 1050°C was again constructed in [20] (Fig. 2). Alloys of 20 compositions over the entire composition range were produced by reactive sintering for 14 days or melted in an arc furnace and annealed for 2 to 7 days depending on composition. The alloys were examined by X-ray diffraction (XRD) and scanning electron microscopy with local electron microprobe analysis (SEM/EMPA). Three stable ternary compounds were found (Table 1): $Mo_{1-x}Fe_xB$ (CrB-type structure), $Mo_{1+x}Fe_{2-x}B_4$ (Ta_3B_4-type structure), and Mo_2FeB_2 (U_3Si_2-type structure [21]). The boride phase of Ti_3P-type structure is assigned with composition $Mo_{0.2}Fe_{2.8}B$ in [20] and is considered to be stable only in a narrow temperature range of 1080–1110°C.

The paper [30] employed thermodynamic modeling to construct the liquidus surface of the Mo–Fe–B system over the entire composition range accounting only for ternary Mo_2FeB_2 and Mo_2FeB_4 compounds and experimentally studied alloys of 20 compositions in the Fe-rich region (above 60 at.% Fe).

The arc-melted alloys were examined in cast state by XRD, SEM/EMPA, and differential scanning calorimetry (DSC). The same authors examined in detail the effect of molybdenum additions within 15 wt.% or 8.1 at.% on the structure of the cast 96.5 wt.% Fe–3.5 wt.% B ($Fe_{84}B_{16}$) alloy and their corrosion resistance to molten zinc in the paper [5].

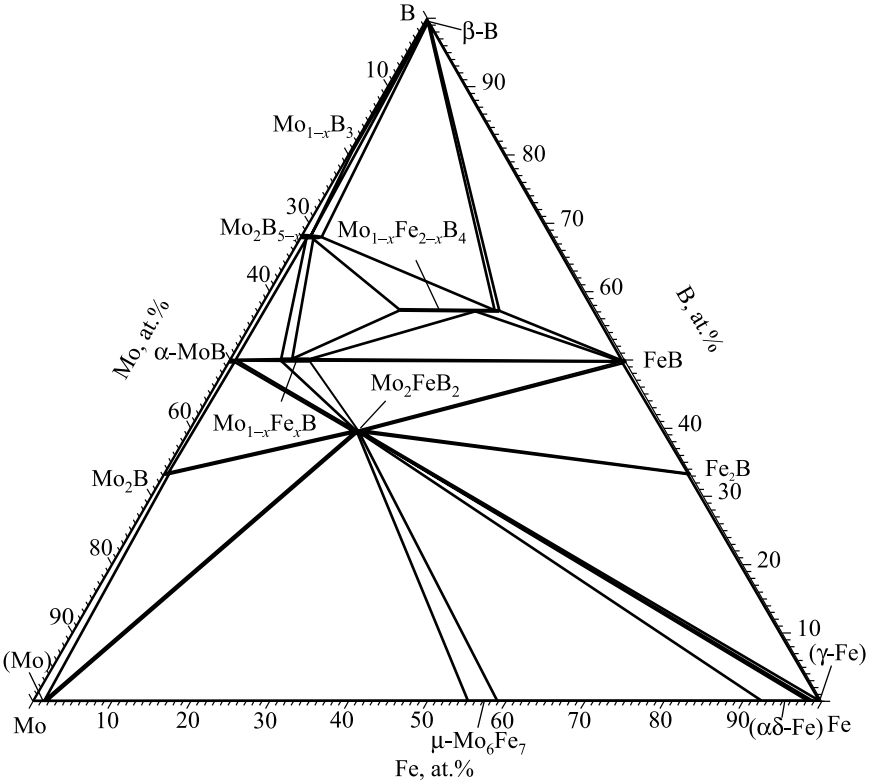

Fig. 2. Isothermal section of the Mo–Fe–B phase diagram at 1050°C [20]

Analysis of the literature data indicates that phase equilibria remain inadequately studied at melting/crystallization temperatures in the Mo–Fe–B ternary system.

The objective of this effort was to study phase equilibria in the Mo–Fe–B system at subsolidus temperatures at boron content varying from 0 to 50 at.% and to construct the solidus surface projection.

EXPERIMENTAL PROCEDURE

To prepare alloys, we used especially pure carbonyl iron, molybdenum powders and rods, and black amorphous boron (with 0.02 wt.% C admixture). The alloys were produced by melting in an electric arc furnace on a water-cooled copper hearth with a nonconsumable tungsten electrode in an argon atmosphere purified from admixtures with a molten titanium getter for 5 min.

Prior to use, the metallic components were melted several times to remove oxides and volatile admixtures from them. Boron and molybdenum were introduced as master alloys prepared in the same conditions. The master alloys were ground and mixed and then melted three to four times. The master alloy compositions were determined by chemical analysis, at.%: 62.7 Fe–37.3 Mo, 51.4 Fe–49.6 B, 52.7 Mo–47.3 B, and 52.9 Fe–34.1 Mo–13.0 B. The master alloys contained the following admixtures found by chemical and spectral analyses, wt.%: 0.02–0.03 O, 0.02–0.03 C, <0.001 H and N, <0.01 Ti, approximately 10^{-3} Ni, Cu, and Si.

The alloys were examined after annealing at subsolidus temperatures. The samples were annealed using SShVL 0.6.2/16 and 0.6.2/25 resistance furnaces. Temperatures of phase transformations were determined by differential thermal analysis (DTA). The annealing temperature was chosen so as to be ~30–50°C lower than the incipient melting temperature. To establish the incipient melting temperature, the pyrometric Pirani–Altertum method was applied. The phase composition of the samples was studied with XRD. The alloy preparation and examination procedures are described in detail in [28, 31]. The microstructure was analyzed with metallographic SEM/EMPA tools employing Jeol electron microprobe analyzers: Superprobe 8200 with a WDX spectrometer and a JAMP 9500 F with an EDX spectrometer.

EXPERIMENTAL RESULTS AND DISCUSSION

The chemical composition of the test alloys, annealing models, and incipient melting temperatures are summarized in Table 2 and XRD results for the key alloys in Table 3. These data were used to construct the solidus surface (Fig. 3*a*–*c*) of the Mo–Fe–B system at boron content ranging from 0 to 50 at.% and establish coordinates of three-phase regions at subsolidus temperatures (Table 4). Analysis of the alloys annealed at subsolidus temperatures revealed that ternary Mo_2FeB_2 (τ_2) boride was in equilibrium with each binary and unary phase existing in the composition range of interest.

Ternary $Mo_xFe_{3-x}B$ Compound. The structure of annealed alloys 1 ($Mo_{10}Fe_{65}B_{25}$) and 3 ($Mo_3Fe_{85}B_{12}$) (Fig. 4*a, b*) and a number of other alloys (Fig. 3*a, c*) determined with XRD and metallography at room temperature

TABLE 2. Incipient Melting Temperatures of Mo–Fe–B Alloys

Sample No.	Alloy composition	Heat treatment mode		Incipient melting temperature of the samples		
		T, °C	τ, h	annealed	cast	
				DTA	pyrometric	DTA
1	$Mo_{10}Fe_{65}B_{25}$	1070	5	1138	–	1130
2	$Mo_{40}Fe_{20}B_{40}$	1880	1	–	1935	–
3	$Mo_3Fe_{85}B_{12}$	1070	5	1146	–	1115
4	$Mo_6Fe_{82}B_{12}$	1070	5	1146	–	1105
5	$Mo_9Fe_{79}B_{12}$	1070	5	1145	–	1105
6	$Mo_{12}Fe_{76}B_{12}$	1150	5	1230	–	1245
7	$Mo_{15}Fe_{73}B_{12}$	1250	5	1284	–	1278
8	$Mo_{18}Fe_{70}B_{12}$	1250	5	1303	–	1302
9	$Mo_{25}Fe_{63}B_{12}$	1250	5	1296	–	1300
10	$Mo_{32}Fe_{56}B_{12}$	1250	5	1298	–	1295
11	$Mo_{37}Fe_{51}B_{12}$	1300	5	1301	–	1281
12	$Mo_{41}Fe_{47}B_{12}$	1300	5	1365	–	1370
13	$Mo_{47}Fe_{41}B_{12}$	1400	5	1450	–	1460
14	$Mo_{56}Fe_{32}B_{12}$	1400	5	1445	–	1449
15	$Mo_{63}Fe_{13}B_{24}$	1400	5	1542	–	1532
28	$Mo_{26}Fe_{67}B_7$	1240	15	1304	1260*	1297
29	$Mo_{33}Fe_{60}B_7$	1240	15	1299	1280	1296
30	$Mo_{45}Fe_{48}B_7$	1290	15	1335*	1335*	1340*
31	$Mo_{80.5}Fe_{12.5}B_7$	1440	20	1451	1830*	1442
32	$Mo_6Fe_{76}B_{18}$	1090	15	1146	1143	1147
33	$Mo_{15}Fe_{67}B_{18}$	1090	15	1145	1136	1145
34	$Mo_{44}Fe_{38}B_{18}$	1290	15	1352*	1346*	1345*
35	$Mo_{17}Fe_{59}B_{24}$	1090	15	1142	1135	1145
36	$Mo_{35}Fe_{41}B_{24}$	1210	15	1303	1243*	1293
37	$Mo_6Fe_{64}B_{30}$	1090	15	1160	1140	1140
38	$Mo_{26}Fe_{44}B_{30}$	1090	15	1153	1120*	1130
39	$Mo_{61}Fe_9B_{30}$	1280	25	1524	1747*	1524
40	$Mo_{17}Fe_{43}B_{40}$	1290	15	1363	1350	1393
41	$Mo_{55}Fe_5B_{40}$	1880	15	–	1940	–

Note. The minus sign indicates that no data are available and an asterisk that the values are overestimated or underestimated.

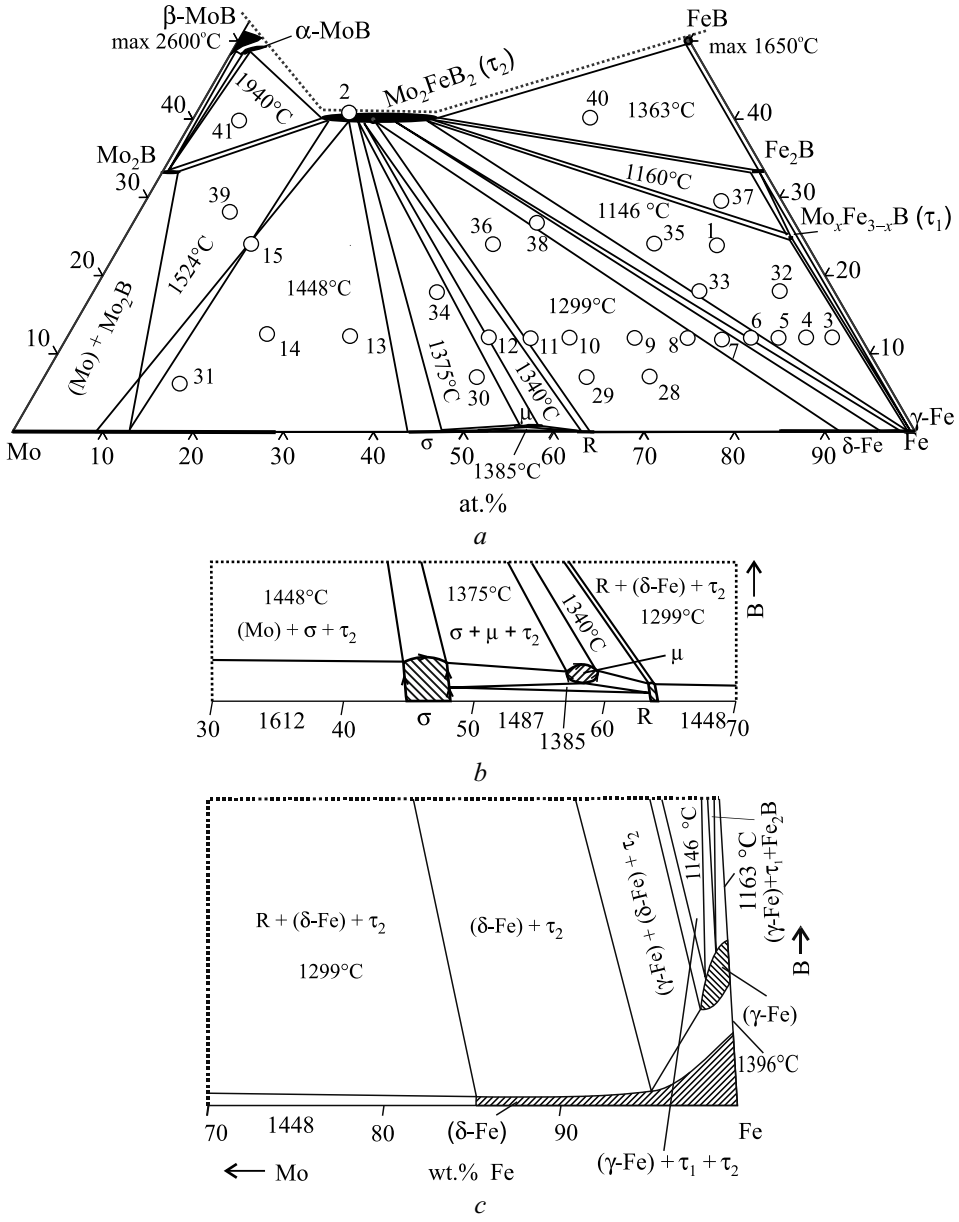

Fig. 3. Solidus surface projection of the Mo–Fe–B system (*a*) and schematic phase equilibria on the solidus surface in the range of intermetallic compounds (*b*) and γ-Fe and δ-Fe-based phases (*c*)

includes an iron-based bcc phase (αδ-Fe), ternary Mo_2FeB_2 (τ_2) boride, and another ternary Fe_3B-based compound, whose composition can be written as $Mo_xFe_{3-x}B$ (τ_1). The DTA curves for annealed alloys 1 and 3 (Fig. 5*a*, *b*) show a temperature effect that corresponds to the polymorphic transformation of the iron-based phase: (α-Fe) + Fe_2B ↔ (γ-Fe) + Mo_2FeB_2. The thermal effect is regularly observed at temperatures close to 890–930°C for a group of alloys 1, 3–5, 32, 33, and 35. According to DTA of the annealed samples, this group has close and quite low incipient melting temperatures, corresponding to four-phase invariant equilibrium involving the melt at 1146 ± ± 4°C. Metallography and XRD indicate that the compositions of these alloys fall into the three-phase (γ-Fe) + Mo_2FeB_2 + $Mo_xFe_{3-x}B$ region on the solidus surface (Fig. 3*a, c*).

The composition of alloy 37 ($Mo_6Fe_{64}B_{30}$) annealed at 1090°C for 15 h falls into the three-phase Mo_2FeB_2 + $Mo_xFe_{3-x}B$ + Fe_2B region (Fig. 4*c*). Two thermal effects are observed on the DTA heating curve (Fig. 5*c*). The effect at 1160°C corresponds to a four-phase invariant region involving the liquid phase and

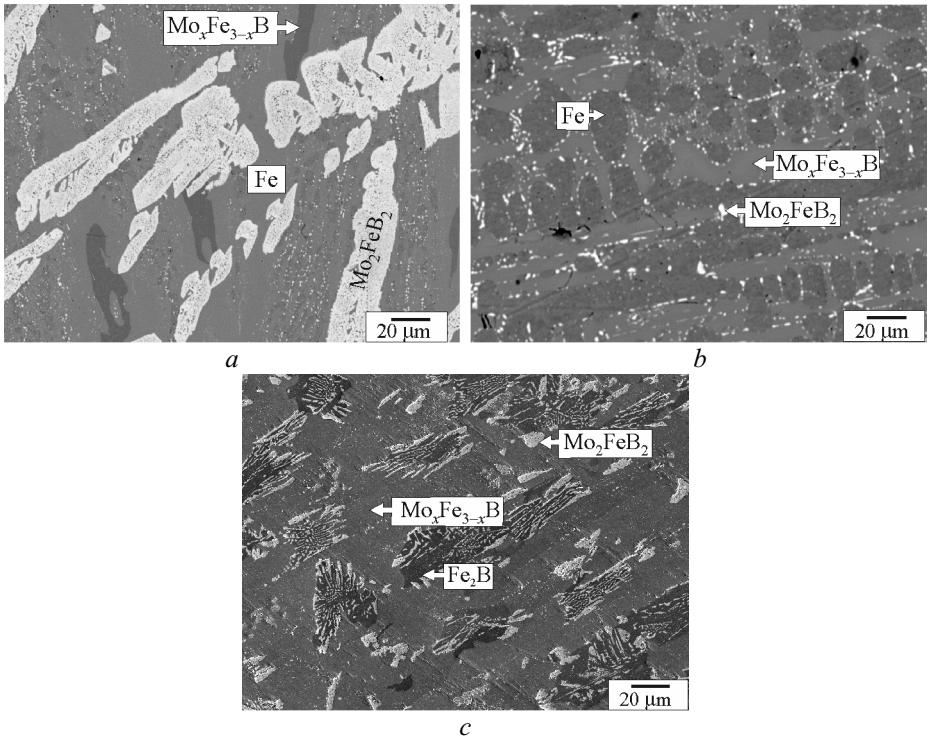

Fig. 4. Microstructure of the annealed Mo–Fe–B alloys (SEM, backscattered electrons) containing the $Mo_xFe_{3-x}B$ phase: *a*) $Mo_{10}Fe_{65}B_{25}$ (1070°C, 5 h); *b*) $Mo_3Fe_{85}B_{12}$ (1070°C, 5 h); *c*) $Mo_6Fe_{64}B_{30}$ (1090°C, 15 h)

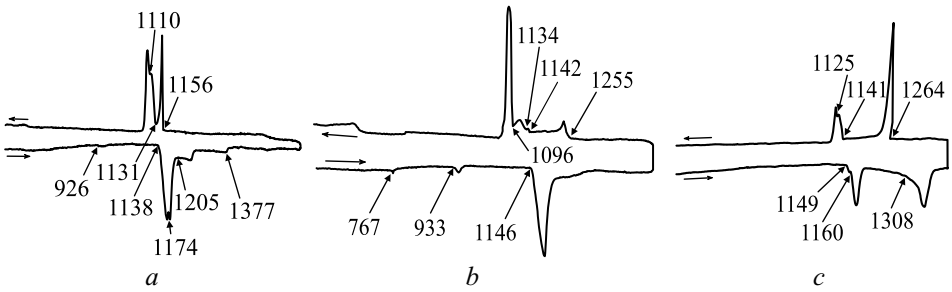

Fig. 5. Differential heating and cooling curves for the annealed Mo–Fe–B samples containing the $Mo_xFe_{3-x}B$ phase: *a*) $Mo_{10}Fe_{65}B_{25}$ (1070°C, 5 h); *b*) $Mo_3Fe_{85}B_{12}$ (1070°C, 5 h); *c*) $Mo_6Fe_{64}B_{30}$ (1090°C, 15 h)

Mo_2FeB_2, $Mo_xFe_{3-x}B$, and Fe_2B borides. The weakest thermal effect at 1149°C corresponds to a four-phase invariant reaction involving the liquid phase in the neighboring three-phase Mo_2FeB_2 + $Mo_xFe_{3-x}B$ + (γ-Fe) region.

According to XRD of the annealed alloys, the $Mo_xFe_{3-x}B$ (τ_1) compound is present in two structural modifications (Table 1): orthorhombic (Fe_3C-type structure) and tetragonal (Ti_3P-type structure); a specific trend of their ratio is difficult to establish. Based on EMPA, $Mo_xFe_{3-x}B$ (τ_1) grains contain 1.3–2.0 at.% Mo. The paper [30] reports that molybdenum content of the τ_1 phase in cast alloys is higher: from 2.4 to 3.9 at.%. The paper [20] indicates that there is a ternary boride of Ti_3P structure and $Mo_{0.2}Fe_{2.8}B$ composition, i.e. with 5 at.% Mo. Hence, the composition of this ternary compound reported in [19] as $Mo_2Fe_{13}B_5$ was not confirmed. The overestimated estimates of molybdenum content in the presence of boron indicated in [20, 30] are probably associated with overlap of molybdenum and boron characteristic radiation.

TABLE 3. Phase Composition of Mo–Fe–B Alloys, According to XRD

Sample No.	Alloy composition	Heat treatment mode		Phase composition		Lattice parameters, pm		
		T, °C	τ, h	Phase	Content, wt.%	*a*	*b*	*c*
1	$Mo_{10}Fe_{65}B_{25}$	1070	5	αδ-Fe	28	286.8(3)	–	–
				$Mo_xFe_{3-x}B$ [Ti_3P]*	37	863.5(9)	–	432.7(6)
				Mo_2FeB_2	36	575.5(6)	–	314.2(4)
2	$Mo_{40}Fe_{20}B_{40}$	1880	1	Mo_2FeB_2	~100	577(1)	–	317.5(6)
5	$Mo_9Fe_{79}B_{12}$	1070	5	αδ-Fe	69	287.2(3)	–	–
				Mo_2FeB_2	26	577.5(6)	–	314.8(4)
				$Mo_xFe_{3-x}B$ [Ti_3P]	5	865(1)	–	438.7(6)
6	$Mo_{12}Fe_{76}B_{12}$	1150	5	αδ-Fe	52	286.9(3)	–	–
				Mo_2FeB_2	48	576.7(7)	–	314.4(4)
7	$Mo_{15}Fe_{73}B_{12}$	1250	5	αδ-Fe	59	288.4(3)	–	–
				Mo_2FeB_2	41	576.8(7)	–	314.3(4)
9	$Mo_{25}Fe_{63}B_{12}$	1250	5	αδ-Fe	30	288.6(3)	–	–
				Mo_2Fe_3	34	1099(2)	–	1931(3)
				Mo_2FeB_2	36	579.6(7)	–	315.0(4)
14	$Mo_{56}Fe_{32}B_{12}$	1400	5	Mo	27	312.3(2)	–	–
				Mo_6Fe_7	32	476.7(5)	–	2571(3)
				Mo_2FeB_2	41	583.8(5)	–	314.1(3)
30	$Mo_{45}Fe_{48}B_7$	1290	15	Mo_6Fe_7	74	477.7 (6)	–	2582(4)
				σ-MoFe	20	924(2)	–	480.3(8)
				Mo_2FeB_2	6	580.9(7)	–	318.2(5)
32	$Mo_6Fe_{76}B_{18}$	1090	15	α-Fe	70	286.6(3)	–	–
				$Mo_xFe_{3-x}B$ [Fe_3C]	20	537.1(8)	666.7(9)	448.7(6)
				Mo_2FeB_2	10	576.3(7)	–	313.8(4)
35	$Mo_{17}Fe_{59}B_{24}$	1090	15	α-Fe	42	286.7(3)	–	–
				$Mo_xFe_{3-x}B$ [Ti_3P]	12	864.4(9)	–	430.0(6)
				Mo_2FeB_2	46	576.4(7)	–	314.1(4)
37	$Mo_6Fe_{64}B_{30}$	1090	15	Fe_2B	23	517.3(6)	–	425.3(5)
				$Mo_xFe_{3-x}B$ [Ti_3P]	18	864.5(9)	–	430.4(5)
				$Mo_xFe_{3-x}B$ [Fe_3C]	48	545.5(7)	679.5(8)	433.8(6)
				Mo_2FeB_2	11	575.9(7)	–	315.2(4)
39	$Mo_{61}Fe_9B_{30}$	1280	15	Mo	10	313.7 (6)	–	–
				Mo_2B	85	553.7(6)	–	472.4(5)
				Mo_2FeB_2	5	584.5(9)	–	314.0(6)
40	$Mo_{17}Fe_{43}B_{40}$	1290	15	Fe_2B	56	511.0(6)	–	423.5(5)
				FeB	10	553.8(7)	294.8(4)	410.2(5)
				Mo_2FeB_2	34	572.1(6)	–	314.5(4)
41	$Mo_{55}Fe_5B_{40}$	~1900	1	Mo_2B	11	555.4(7)	–	472.9(6)
				α-MoB	8	311.0(4)	–	1697(3)
				Mo_2FeB_2	81	584.0(9)	–	319.2(5)

*The phase structural type is indicated.

TABLE 4. Coordinates of the Three-Phase Regions on the Solidus Surface of the Mo–Fe–B System and Comparison of Incipience Melting Temperatures

Phase[1] region	Phase	Phase composition, at.%			Solidus temperature, °C		
		Mo	Fe	B	This paper	According to [30]	
						Experiment	Calculation
α-MoB + β-MoB + Mo_2B	α-MoB	–	–	–	–	–	1942[3]
	β-MoB	–	–	–			
	Mo_2B	–	–	–			
α-MoB + Mo_2B + τ_2	α-MoB	49.2 ± 1.2	0.3 ± 0.2	50.5 ± 1.2	1940 ± 15		
	Mo_2B	68.0 ± 2.1	2.1 ± 0.3	29.8 ± 2.0			
	τ_2	46.3 ± 1.0	13.7 ± 1.0	40.0[2]			
(Mo) + Mo_2B + τ_2	(Mo)	86.6 ± 0.6	13.4 ± 0.6	0.0	1524 ± 15	–	1556
	Mo_2B	68.1 ± 3.5	3.1 ± 0.6	28.8 ± 3.3			
	τ_2	44.7 ± 2.6	14.5 ± 0.8	40.8 ± 3.1			
(Mo) + σ + τ_2	(Mo)	91.7 ± 1.0	8.3 ± 1.0	0.0	1448 ± 10	–	1372
	σ	56.9 ± 0.2	43.1 ± 0.2	0.0			
	τ_2	46.7 ± 1.0	17.6 ± 0.5	35.7 ± 1.3			
σ + μ + R	σ	–	–	–	1385 ± 10	–	1371
	μ	–	–	–			
	R	–	–	–			
σ + μ + τ_2	σ	54.6 ± 0.6	45.4 ± 0.6	0.0	1375 ± 10	–	1330
	μ	43.3 ± 0.5	56.7 ± 0.5	0.0			
	τ_2	44.6 ± 1.5	18.7 ± 0.3	36.7 ± 1.5			
R + μ + τ_2	μ	–	–	–	1340 ± 10	–	1297
	R	–	–	–			
	τ_2	–	–	–			
R + (δ-Fe) + τ_2	δ-Fe	7.0 ± 0.6	93.0 ± 0.6	0.0	1299 ± 5	1255	1257
	R	33.1 ± 0.4	66.8 ± 0.4	0.0			
	τ_2	44.1 ± 2.8	20.1 ± 1.1	35.8 ± 3.5			
(δ-Fe) + (γ-Fe) + τ_2	δ-Fe	~ 4.1	~ 95.9	0.0	–	1250	1241
	γ-Fe	~ 1.3	~ 98.7	0.0			
	τ_2	~ 39.1	~ 22.6	~ 38.3			
(γ-Fe) + τ_1 + τ_2	γ-Fe	0.6 ± 0.1	99.4 ± 0.1	0.0	1146 ± 4	1122[4]	1138[4]
	τ_1	1.6 ± 0.2	72.2 ± 0.8	26.2 ± 0.8			
	τ_2	29.7 ± 2.9	27.2 ± 2.2	43.1 ± 2.4			
Fe_2B + τ_1 + τ_2	Fe_2B	0.8 ± 0.1	62.3 ± 1.9	36.9 ± 2.0	1160 ± 8		
	τ_1	1.4 ± 0.2	69.4 ± 3.0	29.2 ± 3.0			
	τ_2	34.3 ± 1.2	27.0 ± 2.4	38.7 ± 3.2			
(γ-Fe) + Fe_2B + τ_1	γ-Fe	–	–	–	~ 1167		
	Fe_2B	–	–	–			
	τ_1	–	–	–			
Fe_2B + FeB + τ_2	Fe_2B	0.9 ± 0.1	61.7 ± 5.0	37.4 ± 5.0	1363 ± 10	–	1320
	FeB	2.8 ± 0.5	43.4 ± 1.9	53.8 ± 2.1			
	ϑ_2	35.5 ± 2.1	26.3 ± 1.3	38.2 ± 3.4			

[1]Phase notation: τ_1–$Mo_xFe_{3-x}B$, τ_2–Mo_2FeB_2, σ–MoFe, μ–Mo_6Fe_7, R–Mo_2Fe_3. [2]Boron content as per literature data. [3]On assumption of β-MoB + Mo_2B + τ_2 equilibrium. [4]On assumption of (γ-Fe) + Fe_2B + τ_2 equilibrium.

Phase Equilibria Involving Phases Based on δ-Fe and γ-Fe Modifications. The polymorphic modifications of iron at 912 and 1394°C determine specific features of the ternary Mo–Fe–B phase diagram in the iron-rich region. Comparably low melting points in the binary Fe–B system make the iron-based (γ-Fe) phase to participate in phase equilibria at solidus temperatures (Fig. 3*a, c*).

According to XRD, alloy 10 ($Mo_{32}Fe_{56}B_{12}$) annealed at 1250°C for 5 h consists of three phases (Fig. 6*a*): iron-based bcc phase (αδ-Fe), high-temperature intermetallic Mo_2Fe_3 (R phase), and ternary Mo_2FeB_2 (τ_2). The DTA heating curve shows an intensive endothermic effect at 1298°C (Fig. 7*a*), which corresponds to the solidus temperature in the three-phase Mo_2FeB_2 + R-(Mo_2Fe_3) + (δ-Fe) region. The next endothermic effect at 1340°C corresponds to a four-phase invariant reaction involving the melt in the adjacent three-phase Mo_2FeB_2 + R-(Mo_2Fe_3) + μ-(Mo_6Fe_7) region.

The samples of annealed alloys 8 (Fig. 7*b*), 9, 10, 11, 28, 29, and 36 have virtually the same incipient melting temperature, which is 1299 ± 5°C upon the statistical processing of DTA data. The microstructure of annealed alloy 8 ($Mo_{18}Fe_{70}B_{12}$) examined with XRD and metallography (Fig. 6*b*) revealed only two phases:

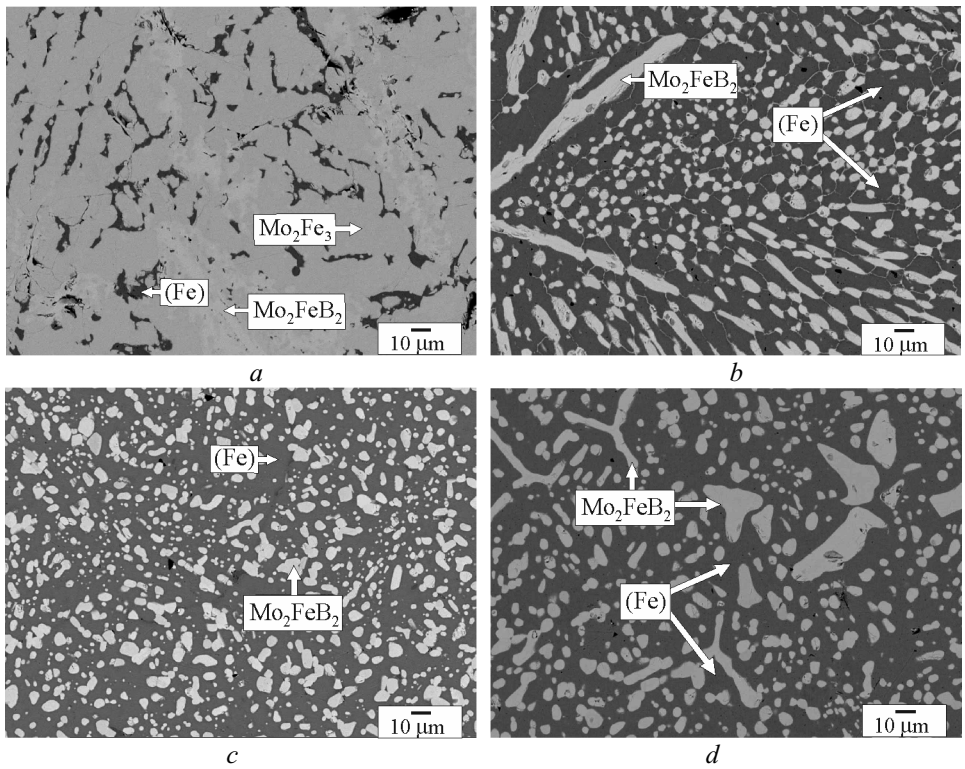

Fig. 6. Microstructure of the annealed Fe-rich Mo–Fe–B alloys (SEM, backscattered electrons): *a*) $Mo_{32}Fe_{56}B_{12}$ (1250°C, 5 h); *b*) $Mo_{18}Fe_{70}B_{12}$ (1250°C, 5 h); *c*) $Mo_{12}Fe_{76}B_{12}$ (1150°C, 5 h), *d*) $Mo_{15}Fe_{73}B_{12}$ (1250°C, 5 h)

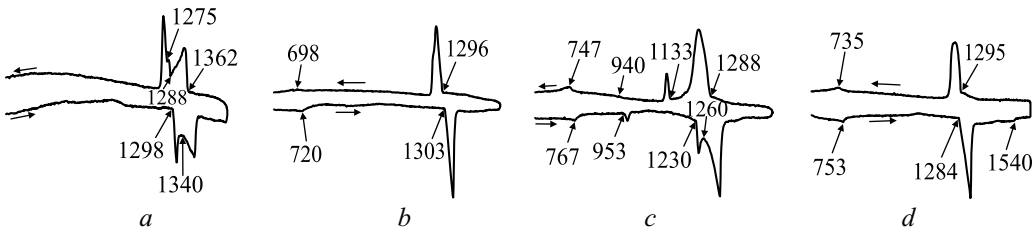

Fig. 7. Differential heating and cooling curves for the annealed Fe-rich Mo–Fe–B alloys: *a*) $Mo_{32}Fe_{56}B_{12}$ (1250°C, 5 h); *b*) $Mo_{18}Fe_{70}B_{12}$ (1250°C, 5 h); *c*) $Mo_{12}Fe_{76}B_{12}$ (1150°C, 5 h), *d*) $Mo_{15}Fe_{73}B_{12}$ (1250°C, 5 h)

Mo_2FeB_2 and (δ-Fe). This indicates that the alloy 8 composition falls into the three-phase Mo_2FeB_2 + (δ-Fe) + R-(Mo_2Fe_3) region close to the Mo_2FeB_2–(δ-Fe) tie-line or that the molybdenum content of the iron-based phase is underestimated because of insufficiently harsh cooling after annealing (Fig. 3*a, c*).

Alloys 7 ($Mo_{15}Fe_{73}B_{12}$) and 6 ($Mo_{12}Fe_{76}B_{12}$) after subsolidus annealing at 1250 and 1150°C, respectively, do not differ from alloy 8 ($Mo_{18}Fe_{70}B_{12}$) in phase composition and microstructure (Fig. 6*c*, *d*). The iron-based phase (δ-Fe) in alloy 7 ($Mo_{15}Fe_{73}B_{12}$) contains ~4.1 at.% Mo and only ~1.3 at.% Mo in alloy 6 ($Mo_{12}Fe_{76}B_{12}$). According to DTA, the incipient melting temperatures of alloys 6–8 decrease with reducing molybdenum content (Fig. 7*c*, *d*). Only does the DTA heating curve for alloy 6 show an endothermic effect below the incipient melting temperature (at 953°C), which can be interpreted as transformation involving the γ-Fe phase: (α-Fe) + Fe_2B → (γ-Fe) + Mo_2FeB_2. This indicates that the composition of alloy 6 falls onto the (γ-Fe)–Mo_2FeB_2 tie-line or close to it and that of alloy 7 onto the (δ-Fe)–Mo_2FeB_2 tie-line (Fig. 3*a, c*).

Analysis of phase equilibria leads to the conclusion that there should be a three-phase (δ-Fe) + (γ-Fe) + Mo_2FeB_2 region between the two-phase (δ-Fe) + Mo_2FeB_2 and (γ-Fe) + Mo_2FeB_2 regions on the solidus surface (Fig. 3*a, c*). After subsolidus annealing, the fcc phase (γ-Fe) does not remain when the samples are cooled with the furnace but transforms to the low-temperature bcc modification (α-Fe). The incipient melting temperature (solidus) in the (δ-Fe) + (γ-Fe) + Mo_2FeB_2 range can be estimated as intermediate between 1230 and 1284°C, which are incipient melting temperatures of annealed alloys 6 ($Mo_{12}Fe_{76}B_{12}$) and 7 ($Mo_{15}Fe_{73}B_{12}$), respectively (Fig. 7*c*, *d*).

Phase Equilibria in Molybdenum-Rich Region. The incipient melting temperature of cast alloy 41 ($Mo_{55}Fe_5B_{40}$) determined by pyrometry is 1940 ± 15°C, which agrees well with thermodynamic calculation [30]. The microstructure of this alloy annealed at 1880°C for 15 h consists of three borides (Fig. 8*a*): binary Mo_2B, ternary Mo_2FeB_2 (τ_2), and α-MoB, phase based on the low-temperature modification of molybdenum monoboride. This indicates that a four-phase invariant equilibrium exists at the solidus temperature. In the binary Mo–B system, phase equilibria involving only one modification of molybdenum monoboride—high-temperature β-MoB—proceed at solidus temperatures. In the ternary Mo–Fe–B system, there is α-MoB + Mo_2B equilibrium on the solidus temperature. This necessitates the existence of a narrow three-phase α-MoB + β-MoB + Mo_2B region located near the Mo–B side of the composition triangle (Fig. 3*a*). The low-temperature modification of molybdenum monoboride, α-MoB, existing as a ternary phase forms in invariant reaction involving the melt. The temperature of this transformation should be higher than the incipient melting temperature in the neighboring three-phase α-MoB + Mo_2FeB_2 + Mo_2B region.

The incipient melting temperature of cast alloy 2 ($Mo_{40}Fe_{20}B_{40}$) determined by pyrometry on cast samples with the Pirani–Altertum method is approximately 1935°C. According to metallography (Fig. 8*b*) and XRD, the alloy annealed resistively at 1880°C for 1 h primarily consists of ternary Mo_2FeB_2 compound and contains a small amount of molybdenum monoboride α-MoB.

For alloy 39 ($Mo_{61}Fe_9B_{30}$), the incipient melting temperature measured by pyrometry is substantially overestimated (1747°C) compared to that determined by DTA as a result of relatively high content of refractory Mo_2B and Mo_2FeB_2 boride phases and low content of a relatively easily fusible molybdenum-based phase. In this case, preference should be given to DTA data (Fig. 9*a*). The heating curve for cast alloy 39 ($Mo_{61}Fe_9B_{30}$) shows two endothermic effects, one (at 1524°C) corresponding to the incipient melting of alloys in the three-phase Mo_2B + (Mo) + Mo_2FeB_2 region, which agrees well with the calculation [30], and the other at 1442°C with the invariant equilibrium involving the melt in the neighboring three-phase (Mo) + Mo_2FeB_2 + σ-(MoFe) region (Fig. 9*a*). After this alloy is annealed at 1500°C for 20 h, massive Mo_2B grains (Fig. 8*c*) and small fractions of the (Mo) phase and ternary Mo_2FeB_2 (τ_2) boride around the Mo_2B grains are observed. The sample of alloy 39 has the same phase composition after annealing at 1280°C for 15 h. Hence, we established the nature of phase equilibria at subsolidus temperatures, including the two-phase (Mo) + Mo_2FeB_2 region. The same result was obtained in [20] for 1050°C (Fig. 2) and in [19] for 1000°C, while the isothermal section at 1000°C with alternative Mo_2B + σ-(MoFe) equilibrium was published in [22].

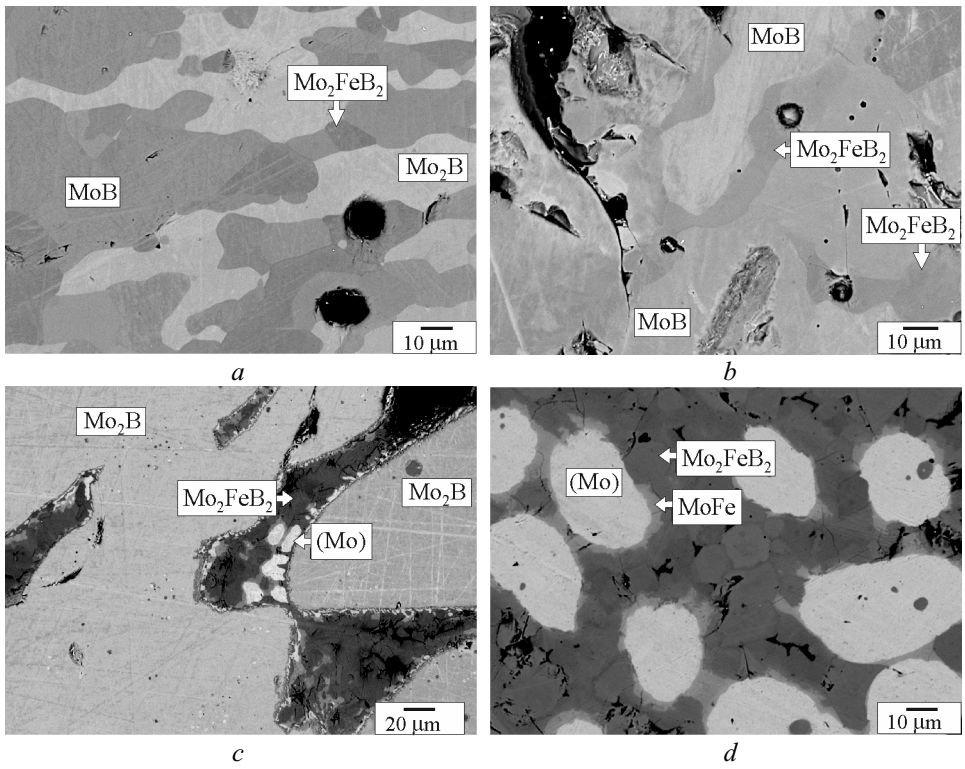

Fig. 8. Microstructure of the annealed Mo-rich Mo–Fe–B alloys (SEM, backscattered electrons): *a*) $Mo_{55}Fe_5B_{40}$ (1880°C, 15 h); *b*) $Mo_{40}Fe_{20}B_{40}$ (1880°C, 1 h); *c*) $Mo_{61}Fe_9B_{30}$ (1500°C, 20 h); *d*) $Mo_{56}Fe_{32}B_{12}$ (1400°C, 5 h)

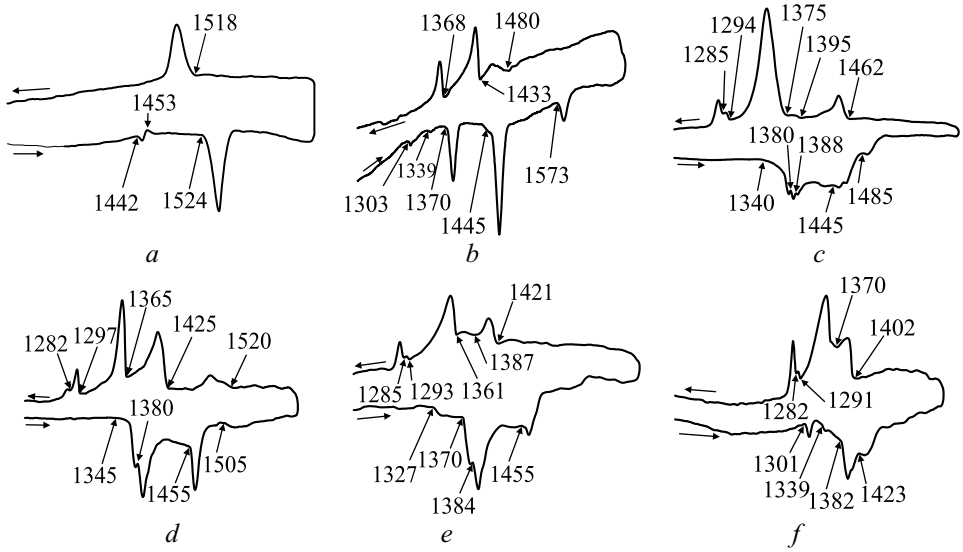

Fig. 9. Differential thermal heating and cooling curves for the annealed Mo–Fe–B alloys: *a*) $Mo_{61}Fe_9B_{30}$ (cast); *b*) $Mo_{56}Fe_{32}B_{12}$ (1400°C, 5 h); *c*) $Mo_{45}Fe_{48}B_7$ (1290°C, 15 h); *d*) $Mo_{44}Fe_{38}B_{18}$ (1290°C, 15 h); *e*) $Mo_{41}Fe_{47}B_{12}$ (1300°C, 5 h); *f*) $Mo_{37}Fe_{51}B_{12}$ (1300°C, 5 h)

The compositions of alloys 13 ($Mo_{47}Fe_{41}B_{12}$) and 14 ($Mo_{56}Fe_{32}B_{12}$) fall into the three-phase (Mo) + Mo_2FeB_2 + σ-(MoFe) region (Fig. 3*a*). According to XRD, alloy 13 annealed at 1400°C for 5 h consists of four phases: σ-(MoFe) + μ-(Mo_6Fe_7) + (Mo) + Mo_2FeB_2, indicating that the σ-(MoFe) phase decomposes when cooled with the furnace. Alloy 14 after the same annealing (Fig. 8*d*) consists of three phases since high-temperature

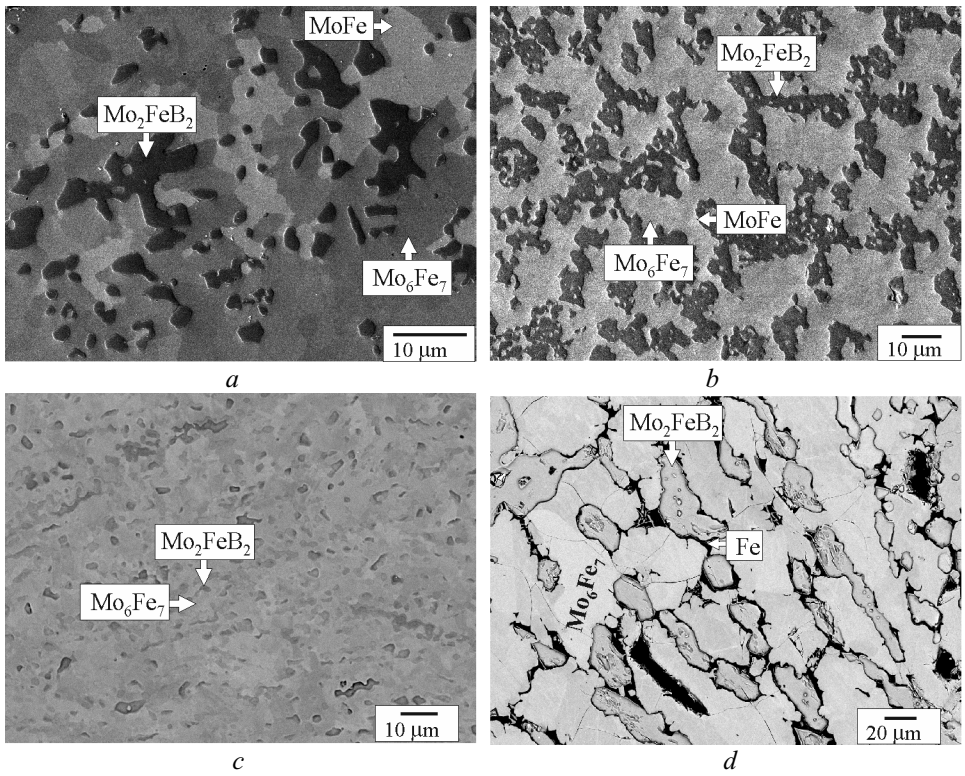

Fig. 10. Microstructure of the intermetallic Mo–Fe–B region (SEM, backscattered electrons): *a*) $Mo_{45}Fe_{48}B_7$ (1290°C, 15 h); *b*) $Mo_{44}Fe_{38}B_{18}$ (1290°C, 15 h); *c*) $Mo_{41}Fe_{47}B_{12}$ (1300°C, 5 h); *d*) $Mo_{37}Fe_{51}B_{12}$ (1300°C, 5 h)

intermetallic σ-(MoFe) decomposes: (Mo) + Mo_2FeB_2 + μ-(Mo_6Fe_7). Based on DTA of annealed alloys (Fig. 9*b*), the incipient melting temperature in the three-phase (Mo) + Mo_2FeB_2 + σ-(MoFe) region is 1448 ± 10°C. The heating and cooling curves for alloys 13 and 14 show cascading thermal effects with repeated temperatures that correspond to four-phase invariant reactions in the neighboring three-phase Mo_2B + (Mo) + Mo_2FeB_2 and σ-(MoFe) + μ-(Mo_6Fe_7) + Mo_2FeB_2 regions and other three-phase regions where the incipient melting temperature is lower. This feature allows one to confidently determine the number of three-phase regions on the solidus surface (Fig. 3*a*, *b*) and get insights into the sequence of four-phase invariant reactions in the Mo–Fe–B system that proceed in the alloy crystallization process.

It is interesting that, according to EMPA of alloys in the three-phase (Mo) + Mo_2FeB_2 + σ-(MoFe) region, iron content of the molybdenum-based phase at subsolidus temperatures is 8.3 ± 1.0 at.%. This is much lower than 13.4 ± 0.6 at.% in the neighboring three-phase Mo_2B + (Mo) + Mo_2FeB_2 region, having higher solidus temperature. This trend is observed for measurements employing two types of microanalyzers: both Superprobe 8200 and JAMP 9500 F (in spite of some differences in the values obtained). These data agree with the solubility of iron in the molybdenum-based phase in the constituent binary Mo–B systems below 1612°C (Fig. 1*a*).

Phase Equilibria in Intermetallic Regions. Four intermetallic phases form in the binary Mo–Fe system: σ-(MoFe), μ-(Mo_6Fe_7), R-(Mo_2Fe_3), and λ-Fe_2Mo. Their close compositions and quite wide homogeneity ranges pose certain difficulties in their identification with SEM/EMPA.

The study of alloys 30 ($Mo_{45}Fe_{48}B_7$) and 34 ($Mo_{44}Fe_{38}B_{18}$) annealed at 1290°C for 15 h by metallography (Fig. 10*a*, *b*) and XRD shows that their compositions fall into the three-phase σ-(MoFe) + μ-(Mo_6Fe_7) + Mo_2FeB_2 region (Fig. 3*a*, *b*). According to XRD and metallography, alloy 12 annealed at 1300°C for 5 h contains practically two phases: μ-(Mo_6Fe_7) + Mo_2FeB_2 (Fig. 10*c*). Based on XRD, alloy 11 after the same annealing consists of two

phases, μ-(Mo_6Fe_7) and Mo_2FeB_2, while metallography (Fig. 10*d*) additionally shows a small amount of the bcc iron-based phase.

Therefore, metallography and XRD uniquely indicate that the intermetallic μ-(Mo_6Fe_7) phase exists in the ternary Mo–Fe–B system at solidus temperatures and is in equilibria with the neighboring binary σ-(MoFe) and R-(Mo_2Fe_3) phases and ternary Mo_2FeB_2 (τ_2) boride (Fig. 3*a*, *b*). The same result was obtained in [30] by thermodynamic calculation.

The three-phase σ-(MoFe) + Mo_2FeB_2 + μ-(Mo_6Fe_7) and μ-(Mo_6Fe_7) + Mo_2FeB_2 + R-(Mo_2Fe_3) planes on the solidus surface of the ternary Mo–Fe–B system lead to the three-phase σ + μ + R region near the Mo–Fe side. Our estimates of phase composition in the ternary system by EMPA indicate that boron has virtually zero solubility in all three intermetallic phases; i.e., the three-phase σ-(MoFe) + μ-(Mo_6Fe_7) + R-(Mo_2Fe_3) region looks like a degenerate triangle with vertices lying almost on one line (Fig. 3*a*, *b*).

In general, we observed a number of repeated thermal effects (Fig. 9*c–f*) that virtually overlap but are reliably separated by DTA in the heating curves for alloys in the intermetallic range, such as 11 ($Mo_{37}Fe_{51}B_{12}$), 12 ($Mo_{41}Fe_{47}B_{12}$), 30 ($Mo_{45}Fe_{48}B_7$), and 34 ($Mo_{44}Fe_{38}B_{18}$). Analysis of the thermal curves for ternary Mo–Fe–B alloys allows the conclusion that these thermal effects are repeated at about 1340, 1370–1380, and 1383–1388°C, indicating that there are three invariant phase reactions at close temperatures and compositions. The three-phase σ-(MoFe) + μ-(Mo_6Fe_7) + Mo_2FeB_2 region corresponds to the four-phase invariant equilibrium involving the liquid phase at 1375 ± 10°C and the incipient melting temperature is 1340 ± 10°C in the three-phase μ-(Mo_6Fe_7) + Mo_2FeB_2 + R-(Mo_2Fe_3) region and 1385 ± 10°C in the σ-(MoFe) + μ-(Mo_6Fe_7) + R-(Mo_2Fe_3) region (Fig. 3*a*, *b*).

Table 4 summarizes our experimental coordinates for the three-phase regions on the solidus surface of the Mo–Fe–B system and compares the incipience melting temperatures with those calculated with the CALPHAD method in [30]. We observed good agreement between the calculated and experimentally measured temperatures in the three-phase regions that are adjacent to the constituent binary Mo–B system. For other parts of the ternary Mo–Fe–B system, the calculation provided underestimated incipient melting temperatures, requiring more accurate thermodynamic data and models to be applied. Our experimental results show that $Mo_xFe_{3-x}B$, α-MoB, and μ-(Mo_6Fe_7) phases (Fig. 3, *a–c*) existing on the solidus surface should be taken into account in thermodynamic modeling of the ternary Mo–Fe–B system and optimization of thermodynamic parameters.

CONCLUSIONS

The solidus surface of the ternary Mo–Fe–B system has been constructed in the region with boron content varying from 0 to 50 at.%, including two-phase (Mo) + Mo_2FeB_2 equilibrium.

Phases based on binary α-MoB and μ-(Mo_6Fe_7) have been established to exist at solidus temperatures in the ternary Mo–Fe–B system.

Ternary $Mo_xFe_{3-x}B$ (τ_1) compound with 1.3–2.0 at.% Mo has been found to exist on the solidus surface and at subsolidus temperatures and ternary Mo_2FeB_2 (τ_2) compound with a wide homogeneity range with iron content varying from 14 to 27 at.% Fe has been confirmed to exist.

The results obtained serve as an experimental basis for optimizing the thermodynamic description of the ternary Mo–Fe–B system, primarily in the Mo–$MoB_{1.0}$–Mo_2FeB_2–FeB–Fe region.

REFERENCES

1. K. Takagi, "Development and application of high strength ternary boride base cermets," *J. Solid State Chem.*, **179**, 2809–2818 (2006).
2. W. Yongguo and L. Zhaoqian, "Development of ternary-boride-based hard cladding material," *Mater. Res. Bull.*, **37**, 417–423 (2002).
3. Zh. Shi, H. Yin, Xu Zh., T. Zhang, G. Yang, Q. Zheng, R. S. Rao, J. Yang, F. Gao, M. Wu, and X. Qu, "Microscopic theory of hardness and optimized hardness model of MX1B and M_2X2B_2 (M = W, Mo; X1 =

Fe, Co, X2 = Fe, Co, Ni) transition-metal ternary borides by the first-principles calculations and experimental verification," *Intermetallics*, **114**, 106573 (2019).
4. S. Akiyama, S. Nakagawa, and M. Naoe, "Electrically conductive layer of wear-resistant Fe–Mo–B alloys for protecting magnetic recording tape," *IEEE Trans. Magn*., **27**, No. 6, 5094–5096 (1991).
5. X. Ouyang, G. Chen, F. Yin, Y. Liu, and M. Zhao, "Effect of molybdenum on the microstructures of as-cast Fe–B alloys and their corrosion resistance in molten zinc," *Corrosion*. **73**, No. 8, 942–952 (2017).
6. Yu.V. Efimov, G.G. Mukhin, Z.G. Fridman, I.S. Bouravleva, and E.A. Myasnikova, "The change of the amorphous state of Fe–Mo–B alloys on heating," *J. Non-Cryst. Solids*, **103**, 45–48 (1988).
7. W. Lingling, Z. Bangwie, Y. Ge, O. Yifang, and H. Wangyu, "Structure and crystallization of amorphous Fe–Mo–B alloys obtained by electroless plating," *J. Alloys Compd*., **255**, No. 1–2, 231–235 (1997).
8. H. Jorgen and V. Nielsen, "Magnetic properties of Fe–Cr–B and Fe–Mo–B metallic glasses," *J. Magn. Magn. Mater*., **19**, No. 1–3, 138–140 (1980).
9. R.A. Dunlap and G. Stroink, "Magnetic properties of amorphous Fe–Mo–B alloys," *Canad. J. Phys*., **62**, 714–719 (1984).
10. E. Dudrova, A. Salak, M. Selecka, and R. Bures, "Properties and microstructure of Fe–1.5 Mo powder steel sintered with a boron-based liquid phase," *Met. Mater*., **33**, No. 2, 60–65 (1985) [Translated from: *Kovove Mater*., **33**, No. 2, 82–93 (1995)].
11. J. Liu, R.M. German, A. Cardamone, T. Potter, and F.J. Semel, "Boron-enhanced sintering of iron-molybdenum steels," *Int. J. Powder Metall*., **37**, No. 5, 39–46 (2001).
12. T.V. Massalski, P.R. Subramanian, H. Okomoto, and L. Kasprzak (eds.), *Binary Alloy Phase Diagrams*, 2nd ed., in 3 vols., ASM International, Materials Park, Ohio (1990), p. 3589.
13. P. Villars and L.D. Calvert, *Pearson's Handbook of Crystallographic Data for Intermetallic Phases*, 2nd ed., 4 vols., ASM International, Materials Park, Ohio (1991), p. 3580.
14. V.B. Rajkumar and K.C. Hari Kumar, "Thermodynamic modelling of the Fe–Mo system coupled with experiments and ab initio calculations," *J. Alloys Compd*., **611**, 303–312 (2014).
15. V.T. Witusiewicz, A.A. Bondar, U. Hecht, O.A. Potazhevska, and T.Ya. Velikanova, "Thermodynamic modelling of the ternary B–Mo–Ti system with refined B–Mo description," *J. Alloys Compd*., **655**, 336–352 (2016).
16. Y. Khan, E. Kneller, and M. Sostarich, "The phase Fe_3B," *Z. Metallkd*., **73**, No. 10, 624–626 (1982).
17. M. Hansen and K. Anderko, *Constitution of Binary Alloys*, McGraw-Hill, New York (1958).
18. P. Rogl and J.C. Schuster, "Mo–B–N (molybdenum–boron–nitrogen)," in: *Phase Diagrams of Ternary Boron Nitride and Silicon Nitride Systems*, Monograph Series on Alloy Phase Diagrams, ASM International, Materials Park, Ohio (1992), pp. 64–67.
19. H. Haschke, H. Nowoyny, and F. Benesovsky, "Investigation in ternary systems: {Mo, W}–{Fe, Co, Ni}–B," *Monatsh. Chem*., **97**, No. 5, 1459–1468 (1966).
20. A. Leithe-Jasper, H. Klesnar, P. Rogl, M. Komai, and K.I. Takagi, "Reinvestigation of isothermal section in M(M = Mo,W)–Fe–B ternary systems at 1323 K," *J. Jpn. Inst. Met*., **64**, No. 2, 154–162 (2000).
21. W. Rieger, H. Nowotny, and F. Benesovsky, "The crystal structure of Mo_2FeB_2," *Monatsh. Chem.*, **95**, 1502–1503 (1964).
22. E.I. Gladyshevskii, T.F. Fedorov, Yu.B. Kuzma, and R.V. Skolozdra, "Isothermal section of the molybdenum–iron–boron system," *Powder Metall. Met. Ceram.*, **5**, No. 4, 305–309 (1966).
23. A.F. Guillermet, "The Fe–Mo (iron–molybdenum) system," *Bull. Alloy Phase Diagrams*, **3**, No. 3, 359–367 (1982).
24. N.P. Lyakishev (ed.), *Phase Diagrams of Binary Metallic Systems* [in Russian], Mashinostroenie, Moscow (1997), Vol. 2, p. 1024.
25. N.P. Lyakishev (ed.), *Binary Phase Diagrams* [in Russian], Mashinostroenie, Moscow (1996), Vol. 1, p. 245.
26. Y. Khan, E. Kneller, and M. Sostarich, "Stability and crystallization of amorphous iron-boron obtained by quenching from the melt," *Z. Metallkd*., **72**, No. 8, 553–557 (1981).

27. V.T. Witusiewicz, A.A. Bondar, U. Hecht, A. Theofilatos, N.I. Tsyganenko, S.V. Utkin, and I.B. Tikhonova, “Experimental study and thermodynamic re-modelling of the constituent binaries and ternary B–Fe–Ti system,” *J. Alloys Compd*., **800**, 419–449 (2019).
28. S.V. Utkin, V.Z. Kublii, S.V. Sleptsov, A.A. Bondar, P.P. Levchenko, G.A. Osokin, and T.Ya. Velikanova, “Solidus surface of the Mo–Ni–B,” *Nadtverd. Mater.*, **41**, No. 5, 3–19 (2019).
29. K. Korniyenko and A. Bondar, “Boron–iron–molybdenum,” in: *Landolt-Börnstein: Numerical Data and Functional Relationships in Science and Technology (New Series)*, W. Martinsen (ed.), Group IV: Physical Chemistry, G. Effenberg and S. Ilyenko (eds.), Ternary Alloy Systems, Phase Diagrams, Crystallographic and Thermodynamic Data Critically Evaluated by MSIT, Springer-Verlag, Berlin, Heidelberg (2007), Vol. 11D1, pp. 354–367.
30. X. Yang, F. Yin, J. Hu, M. Zhao, and Y. Liu, “Experimental investigation and thermodynamic calculation of the B–Fe–Mo ternary system,” *Calphad*, **59**, 189–198 (2017).
31. T.Ya. Velikanova, A.A. Bondar, and A.V. Grytsiv, “The chromium–nickel–carbon phase diagram,” *J. Phase Equilib.*, **20**, No. 2, 125–147 (1999).